Journal of Advanced Ceramics
2023, **12**(7): 1345–1360
https://doi.org/10.26599/JAC.2023.9220759

ISSN 2226-4108
CN 10-1154/TQ

Research Article

Propulsion tests on ultra-high-temperature ceramic matrix composites for reusable rocket nozzles

Diletta Sciti[a], Antonio Vinci[a,*], Luca Zoli[a], Pietro Galizia[a], Simone Failla[a], Stefano Mungiguerra[b,*], Giuseppe D. Di Martino[b], Anselmo Cecere[b], Raffaele Savino[b]

[a]*Institute of Science, Technology and Sustainability for Ceramics—National Research Council, Faenza 48018, Italy*
[b]*Department of Industrial Engineering, University of Naples Federico II, Naples 80125, Italy*

Received: February 6, 2023; Revised: April 4, 2023; Accepted: April 24, 2023

Abstract: Ultra-high-temperature ceramic matrix composites (UHTCMCs) based on a ZrB_2/SiC matrix have been investigated for the fabrication of reusable nozzles for propulsion. Three de Laval nozzle prototypes, obtained by sintering with either hot pressing (HP) or spark plasma sintering (SPS), were tested 2–3 times in a hybrid rocket motor for proving reusability. Sections were extracted after oxidation tests to study the microstructural changes and oxidative and thermomechanical stresses induced by the repeated tests. Compared to a reference graphite nozzle, no measurable erosion was observed for the UHTCMC-based nozzles. The oxidation mechanism consisted in the formation of a ZrO_2 intermediate layer, with a liquid silicon oxide (SiO_2) layer on the surface that was displaced by the action of the gas flux towards the divergent part of the nozzle, protecting it from further oxidation. Both specimens obtained by HP and SPS displayed similar performance, with very slight differences, which were attributed to small changes in porosity. These tests demonstrated the capability of complex-shaped prototypes made of the developed UHTCMCs to survive repeated exposure to environments representative of a realistic space propulsion application, for overall operating time up to 30 s, without any failure nor measurable erosion, making a promising step towards the development of reusable rocket components.

Keywords: ultra-high-temperature ceramics (UHTCs); ceramic matrix composites (CMCs); propulsion; oxidation resistance; nozzle prototypes

1 Introduction

Reusability is considered the key breakthrough needed to reduce the cost of access to space. It is now estimated that reusable launch systems (RLSs) or reusable launch vehicles (RLVs) should reduce manufacturing costs by about 30% [1], by limiting the cost of refurbishing. According to Space X philosophy, reusable rockets will enable people to live on other planets. Reusability of complex systems implies that materials facing high-enthalpy fluxes, thermal shock, unsteady vibrations and shock waves, and extreme heat transfer and surface pressures must be able to self-protect/self-heal with

* Corresponding authors.
E-mail: A. Vinci, antonio.vinci@istec.cnr.it;
S. Mungiguerra, stefano.mungiguerra@unina.it

no/negligible consumption. Two typical environments, where materials are exposed to such harsh conditions, are propulsion and re-entry. During re-entry in an atmosphere from interplanetary missions, thermal protections for vehicles flying at Mach number = 5 or above must withstand extreme temperatures, due to the impact with the atmosphere and the aggressive action of dissociated oxygen and nitrogen [2]. Inside rocket engines, the inner surface of the exhaust nozzle, where the propellant is accelerated to supersonic conditions, is exposed to the highest shear stress, pressure, and heat flux among all the motor components, coupled with a chemically aggressive environment [3]. The combination of extremely harsh thermo-fluid-dynamic and chemical conditions achieved inside the combustion chamber and through the exhaust nozzle of rocket engine sets demanding requirements for advanced materials. These harsh conditions usually lead to material erosion and nozzle throat section increase with a consequent decrease of the combustion chamber pressure and detrimental effects over the motor operation and performance [4,5].

Nowadays, available C/SiC materials can withstand severe conditions at a high temperature (around 1500 ℃), owing to the introduction of ceramic thermal barrier coatings (TBCs), resulting in extraordinary efficiency and performance gains [6–9]. Above this temperature, however, new materials must be designed and developed. Interesting advances have been done in the study of C/C composites protected by ultra-high-temperature ceramic (UHTC) coatings with high thermal conductivity, k_{th} [10], but coatings suffer from coefficient of thermal expansion (CTE, α) mismatch with the underlying material already in the as-fabricated material, and spalling is one major drawback of this technology. For this reason, the scientific community is devoting a considerable effort in the development of a new class of materials, called the ultra-high-temperature ceramic matrix composites (UHTCMCs). UHTCMCs arise from the combination of UHTCs (e.g., borides and carbides of early transition metals) and carbon fibers (C_f) [11,12]. The same material has twofold functions:

(1) In the bulk, fibers provide the structural stability and damage tolerance to the components [13–15].

(2) In the surface, the matrix provides protection for the fibers, forming a protective layer upon exposure to aggressive environments [16] without the use of an external coating. Through an appropriate composite design, UHTCMCs can be used in the production of near-zero erosion nozzles, and near-zero ablation TPS tiles up to unprecedented levels, e.g., for temperatures > 1800 ℃ [17–19]. Different techniques are currently in use for the production of UHTCMCs, most of them relying on the same techniques used for conventional CMCs and requiring the use of expensive fiber coatings. PIP-based materials have excellent damage tolerance [20–23] and enhanced properties but lower high-temperature resistance (above 1600 ℃) due to high contents of SiC-based phases [22,24–26]. Chemical vapour infiltration (CVI) composites have the highest mechanical properties [22,24,25,27–29], but processing is quite time-consuming because they require the use of gaseous precursors of C and SiC as raw materials [30–32]. Liquid silicon infiltration and its evolution in reactive metal infiltration pose the problem of coating to protect the C_f preform from reaction with the molten metal and of residual unreacted metal, which could worsen the mechanical and oxidation resistance [33–35].

We have proposed a different approach, where the C preforms are perfectly and homogeneously integrated into an ultra-refractory-sintered ceramic matrix. Neither coating nor external TBC is applied to the fiber. This approach was widely developed during the European Union (EU) project C^{3}HARME [36,37]. Sintering of these UHTCMCs through methods typical of bulk ceramic science (e.g., hot pressing (HP) and spark plasma sintering (SPS) [38]) is the key processing step that distinguishes these non-oxide/C_f composites from their predecessors [39]. The chosen ceramic matrix consists of ZrB_2 with the addition of 10% SiC. ZrB_2 is the most appealing choice among borides because of its lower density and cost, coupled with a melting point above 3000 ℃, high thermal conductivity, and good high-temperature strength [40]. SiC was added as the sintering aid and also to promote the formation of a silica-based glass under oxidation, which improves the oxidation resistance of the boride matrix [41]. Reference [42] has demonstrated that these composites can be efficiently scaled-up without significant variations of microstructure and thermomechanical properties and indistinctly processed by either HP or SPS.

In this work, an extensive campaign of propulsion tests on UHTCMC nozzles was carried out, including three de Laval nozzle prototypes, each tested 2–3 times in a hybrid rocket motor for proving reusability. All the nozzles were machined from HPed and SPSed UHTCMCs. Sections were extracted after reusability tests to analyze the microstructural changes and oxidative and thermomechanical stresses induced by repeated tests.

2 Materials and methods

2. 1 Material preparation

The following raw materials were used: ZrB_2 (Grade B, H.C. Starck, Germany), specific surface area: 1.0 m^2/g, particle size range: 0.5–6 μm, impurities (wt%): 0.25 C, 2.00 O, 0.25 N, 0.10 Fe, and 0.20 Hf; α-SiC (Grade UF-25, H.C. Starck, Germany), specific surface area: 23–26 m^2/g, D_{50}: 0.45 μm; and commercial high-modulus pitch-derived C_f preforms (TCU312 supplier, Angeloni S.r.l., Italy). For the matrix of UHTCMCs, ZrB_2/SiC powder mixtures were prepared by wet ball milling and drying. With these mixtures, water-based slurries were prepared using polyacrylates at different molecular weights as dispersants to adjust the fiber volumetric amount [37,43]. The composites were fabricated by infiltrating the fabrics with the slurries with subsequent stacking in a predefined sequence and sintering by HP or SPS at temperatures between 1800 and 1930 ℃ under 30 MPa pressure. The microstructures were analyzed on polished and fractured surfaces by the field emission scanning electron microscope (FE-SEM; Sigma NTS GmbH, Carl Zeiss, Öberkochen, Germany) and energy dispersive X-ray spectrometer (EDS; INCA Energy 300, Oxford instruments, Oxford, UK). After sintering, the bulk density was determined by the Archimedes' method. The relative density, ρ, was calculated as the ratio of experimental to theoretical value, and the residual porosity was obtained as $(1-\rho)$. The theoretical densities of the materials were calculated using the rule of mixture on the basis of the starting compositions. The densified UHTCMCs were machined to the final shape, according to the sketches presented in Fig. 1. Three samples were produced and were labelled as HP-2, HP-3, and SPS-2, where the first letters identify the sintering method (HP or SPS), and the number identifies the number of times the sample tested.

2. 2 Propulsion tests

The test facility is a versatile experimental setup primarily designed for firing hybrid rocket engines of several sizes [44]. The equipment includes a test rig and a general-purpose data acquisition system, which allows performing several types of tests. Gaseous oxygen was supplied by a reservoir of six cylinders; the operating pressure along the motor feed line was set by means of an electronically controlled pressure valve (ER3000, TESCOM). The oxygen mass flow rate was evaluated through gas temperature and pressure measurements upstream of the throat of a chocked Venturi tube. Nitrogen was purged into the chamber for the burn out and in case of an emergency shutdown.

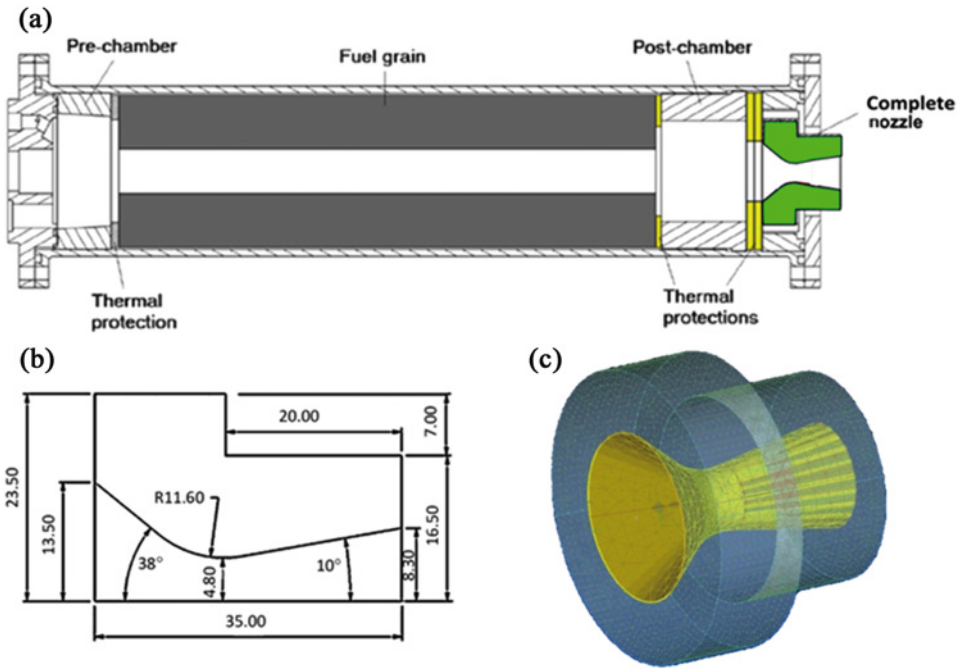

Fig. 1 Schematics of (a) testing chamber, (b) nozzle profile (unit: mm), and (c) nozzle prototype.

The 200-N class hybrid rocket employed in this study, mounted on the test bench, is depicted in Fig. 1. The rocket has an axisymmetric combustion chamber, with 350-mm length and 69-mm inner diameter. The motor forward closure accommodates a converging nozzle injector, whose exit-section diameter is 6 mm.

For the present work, gaseous oxygen was employed as the oxidizer, while a cylindrical grain of solid high-density polyethylene (HDPE) was the fuel. The grain length was 220 mm, and its initial port diameter was 15 mm, with a subsequent increase during burning because of solid fuel consumption. A nominal oxidizer mass flow rate of 40 g/s was chosen. The fuel mass loss was evaluated by weighting the grain before and after test by means of an electronic balance (1 g accuracy), and then the time-averaged fuel mass flow rate was calculated dividing this value by the effective test duration. The oxidizer-to-fuel ratio (O/F) was finally obtained as the ratio between oxygen and HDPE mass flow rates. Upstream and downstream of the solid grain, a dump plenum (25 mm in length and with 44 mm inner diameter) and an aft-mixing chamber (58 mm in length and with 45 mm inner diameter) were set up, respectively. In a typical hybrid rocket test, a graphite converging–diverging nozzle with 9.6-mm throat diameter and an area expansion ratio equal to 2.99 are employed. In the present test campaign, this component was replaced with the UHTCMC, having the same dimensions of the conventional graphite nozzle.

The chamber pressure was measured with two transducers (C206, Setra), which were set up in the prechamber and in the aft-mixing chamber. Furthermore, the rocket was supported on the test bench with four load cells, which allowed evaluating the motor thrust by computing the sum of the loads measured with each cell. The analog signals generated by thermocouples, pressure transducers, and load cells were sampled at 5 kHz, digitally converted, processed, and recorded on the hard disk by a standard system (PXI Express, National Instruments, Austin, USA) interconnected with the computer by means of fiber optic connections. All the signals were stored in a binary format for post-processing and in a text format after downsampling the data to 100 Hz with a boxcar average. All diagrams in Section 3 show the downsampled data.

2. 3 Numerical models

In order to provide a better understanding of test conditions on the prototypes, the computational fluid dynamic (CFD) simulations of the flow through the rocket nozzle were performed, employing as boundary conditions of the time-averaged results of a one-dimensional (1D) numerical tool for the simulation of the conditions in the combustion chamber, described in Ref. [45]. The CFD model herein described was already successfully employed for the simulation of the present hybrid rocket configuration [4,46,47]. To this purpose, the Reynolds-averaged Navier–Stokes (RANS) equations for single-phase multicomponent turbulent reacting flows were solved with a control-volume-based technique and a density-based algorithm [48], employing the shear stress transport (SST) k–ω model as turbulence closure [49]. A detailed analysis of thermo-chemical evolution of gas mixture was performed in order to have an accurate prediction of heat transfer at solid walls. The transport equations for the main combustion products (O_2, C_2H_4, H_2O, CO_2, CO, H_2, H, O, and OH were the species considered in the current model, together with the non-reacting N_2) were solved, and the eddy dissipation concept (EDC) model [50] was employed for the combustion mechanism, which accounts for detailed chemical reaction rates in turbulent flows. More details about the chemical model can be found in Ref. [45]. The discrete ordinate model [51] for the radiation was included in the numerical modelling. The computational grid for the simulation of the flow field through the exhaust nozzle of the hybrid rocket is shown in Fig. 2. A pressure inlet boundary condition was set on the inlet section of the nozzle, imposing the time-averaged values of the total pressure, the total temperature, and the chemical

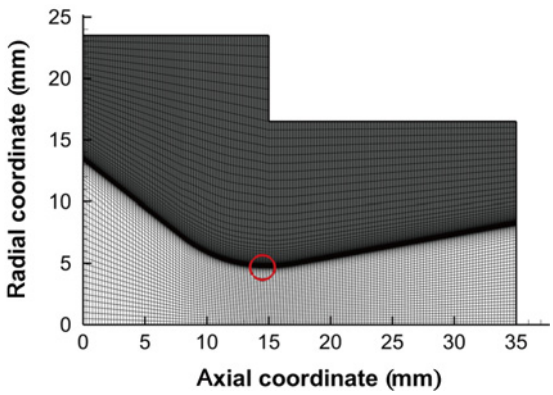

Fig. 2 Computational domain used for numerical simulations of flow field throughout tested nozzles. The picture also shows the mesh used for the thermal simulation of the nozzle prototype (in dark grey). The red circle highlights the area, where the highest heat flux and temperature are expected.

composition estimated by means of the above-mentioned 1D model. A supersonic outlet condition was set at the exit section.

Finally, for the thermal analysis of the solid sample, the time-dependent temperature field inside the sample and its supporting elements were computed solving the energy equation in the solid domain. The distribution of the thermo-fluid dynamic quantities and the chemical compositions in the fluid area near the solid material, and subsequently the convective heat flux, are influenced by the temperature on the exposed surface of the sample. For these reasons, an accurate approach is the one considering the interaction between the fluid and the materials. The thermal coupling condition was set on the interfaces between fluid and solid domains, which is temperature and heat flux continuities. Figure 2 also shows the mesh used for the simulation of the solid nozzle (in dark grey). On the top left and central vertical walls an adiabatic boundary condition was set (since these walls are enclosed within the thermal protections of the engine); while for the two remaining external surfaces, radiation towards a cold environment (T = 300 K) was allowed. Thermodynamic simulations were carried out with FactSage 8.0 software.

2. 4 Post-test characterization

The nozzle throat diameters were measured before and after each test by means of a digital calliper.

The nozzles were machined after propulsion tests to extract portions of the inner profile for inspection. These cross sections were analyzed by the optical microscope (HIROX), and the frontal part and profile of the throats were analyzed by the SEM–EDS.

3 Results and discussion

3. 1 Microstructure of as-sintered specimens

Nozzles were machined from three distinct pellets sintered either by HP or SPS. Features of the as produced specimens were already presented in Refs. [42,52] and were very similar amongst each other. The basic microstructures/textures of the samples are reported in Fig. 3. The microstructure was nearly fully dense, with C_f homogeneously integrated with the ceramic matrix (Fig. 3(a)). The density (~3.6 g/cm^3) was intermediate between that of UHTC (~6 g/cm^3) and of C/SiC composite (~2 g/cm^3). According to the image analysis, $(1-\rho)$ was < 6% for all the specimens (Fig. 3(b)). The composites were nearly flawless apart from local matrix microcracks with a spacing of 20 μm and a thickness below 0.5 μm, transverse to the fiber axis [52,53]. These crack patterns developed during cooling down from densification because of residual stresses arising from thermal expansion mismatch between matrix ($\approx 7.5\times10^{-6}$ ℃$^{-1}$ from room temperature (RT) to 800 ℃ [54]) and fiber along its axis (−1.4 at RT and 1.4×10^{-6} ℃$^{-1}$ at 1500 ℃ [55]) [53]. The sintering conditions used for the fabrication of these composites led to a strong interaction between the fiber and the matrix, as evidenced in Fig. 3(c), where small inclusions of ZrB_2 and SiC can be found embedded in the fiber's surface; these are hypothesized to form from the recrystallization of ZrB_2 grains and from the carbothermal reduction of silicon oxide (SiO_2) present on the starting SiC powders [42]. Although a degradation of the fiber mechanical properties cannot be ruled out, the bending strength and toughness of the uncoated pitch-based carbon fiber-reinforced ZrB_2/SiC composite were comparable to those of the same composite reinforced with coated C_f, leading to the conclusion that pitch-derived C_f can provide toughening even in the absence of a coating thanks to their layered structure that allows intra-fiber pull-out [13,56]. Furthermore, it was observed that the pressure-assisted sintering process did not alter the distribution of fiber diameter in comparison to the PIP process; for coated fibers, > 60% of the total fiber amount was found as fiber clusters with weak inter-fiber interfaces; while for uncoated fibers, up to 40% of the fibers were dispersed into the matrix as single filaments characterized by strong interfaces due to mechanical interlocking thanks to the better slurry infiltration of the fiber bundles [52]. Finally, the composite's overall α gradually approached that of bare C_f as the matrix was gradually damaged [15,53].

Typical thermo-mechanical properties of sintered UHTCMCs are summarized in Table 1 and were obtained by testing rectangular bars machined from specimens produced at different scales [42]. Compared to secondary organic aerosol (SoA) C/SiC composites, UHTCMCs featured higher values of Young's modulus, E, CTE, and thermal conductivity, while the RT strength properties were lower mainly due to the less performing fiber/matrix interface in sintered systems. However, UHTCMCs showed unparalleled properties at elevated temperature (1600–1800 ℃). The strengths (flexural

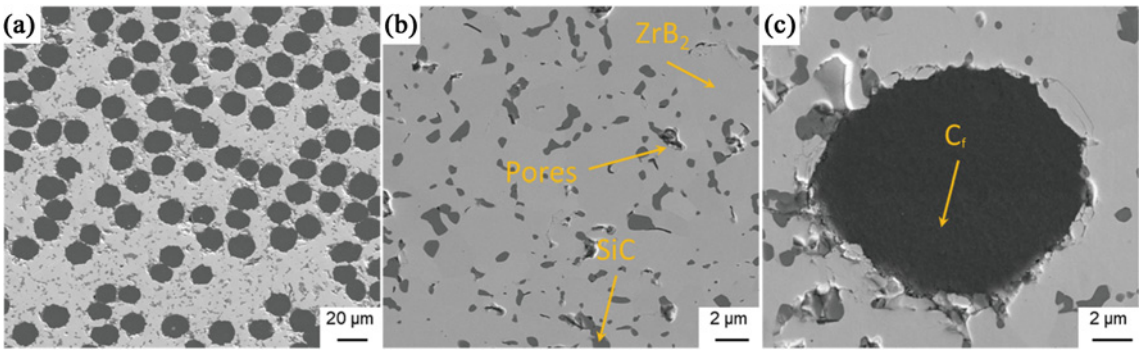

Fig. 3 Microstructures of ZrB_2/SiC–C_f composite sintered by SPS as examples: (a) fiber distribution, (b) detail of matrix, showing SiC (dark grey), ZrB_2 (light grey), and pores, and (c) detail of fiber/matrix interface.

Table 1 Typical thermo-mechanical properties of sintered UHTCMCs compared to those of SoA C/SiC composites

Property	UHTCMCs (averaged)	C/SiC		
		PIP [57]	LSI [58,59]	CVI [59]
Architecture	0°/90°	0°/90°	Two-dimensional (2D)	2D
Density (g/cm^3)	3.7±0.3	1.8	1.8–2.4	2.1–2.2
Porosity (%)	7±4	10	< 1–2	10–15
Fiber amount, V_f (%)	47±7	46	—	42–47
RT E (GPa)	138±17 25±3[a]	65 —	50–80 —	90–100 —
RT shear modulus, G (GPa)	27±7	—	—	—
RT σ_f (MPa)	220±42 23±9[a]	500 —	80–230 —	450–500 —
σ_f at 1800 ℃ (MPa)	307±68	—	—	—
RT tensile strength, σ_t (MPa)	120±7	250	40–350	300–380
σ_t at 1600 ℃ (MPa)	200±24	266	—	—
σ_t at 1800 ℃ (MPa)	200	—	—	—
RT fracture toughness, K_{IC} (MPa·m$^{0.5}$)	9.7±1.1	—	—	—
α (10^{-6} ℃$^{-1}$)	4.2±0.1 8.0±0.4[a]	1.2–2.7 4.1–6.2[a]	3 —	3 —
RT k_{th} (W/(m·K))	140.0 28.1[a]	11.3 5.2[a]	13–40 —	5 —
k_{th} at 1200–1500 ℃ (W/(m·K))	108.3 23.6[a]	12.2 5.3[a]	20 —	5 —

[a] Properties along the pile-up direction

and tensile) at elevated temperatures were always higher than those at RT. Properties were also highly anisotropic along the sample thickness, which is quite relevant for this kind of application. Worthy to note, the CTE along the thickness is twice as high as the in-plane CTE, and the flexural strength, σ_f, modulus, and thermal conductivity are highly reduced through the thickness.

3. 2 Propulsion tests

The three nozzles, labelled as SPS-2, HP-2, and HP-3, were repeatedly tested by means of the subscale hybrid rocket engine, according to the conditions summarized in Table 2. SPS-2 and HP-2 were tested 2 times (Table 2), and the tests had duration of 10 and 15 s for an overall duration of 25 s. HP-3 was tested 3 times, and each test lasted 10 s, for overall engine operation of 30 s.

The shape and size of the UHTCMC nozzle (Fig. 4(a)) are the same as those of the graphite nozzles conventionally used in the laboratory, having a throat diameter of 9.6 mm, with a curvature radius of 11.6 mm and an expansion area ratio of 2.99. The combination of extremely harsh thermo-fluid-dynamic and chemical

Table 2 Consolidation methods, ρ, porosities, test duration, and numbers of tests per specimen. Oxide layer thickness: SPS-2 and HP-2 were tested twice for overall engine operation of 25 s, while HP-3 was tested 3 times for a total of 30 s. The final oxide thickness in the convergent part of the nozzle was measured for each sample

Sample	ρ (g/cm^3)	Porosity (vol%)	No. of tests	Duration (s)				Maximum pressure (bar)			Oxide thickness (μm)
				Test 1	Test 2	Test 3	Total	Test 1	Test 2	Test 3	
SPS-2	3.64	10.8	2	10	15	—	25	10.5	11.0	—	59±10
HP-2	3.74	8.4	2	10	15	—	25	10.2	10.8	—	36±11
HP-3	4.05	0.8	3	10	10	10	30	9.6	9.9	10.2	87±27

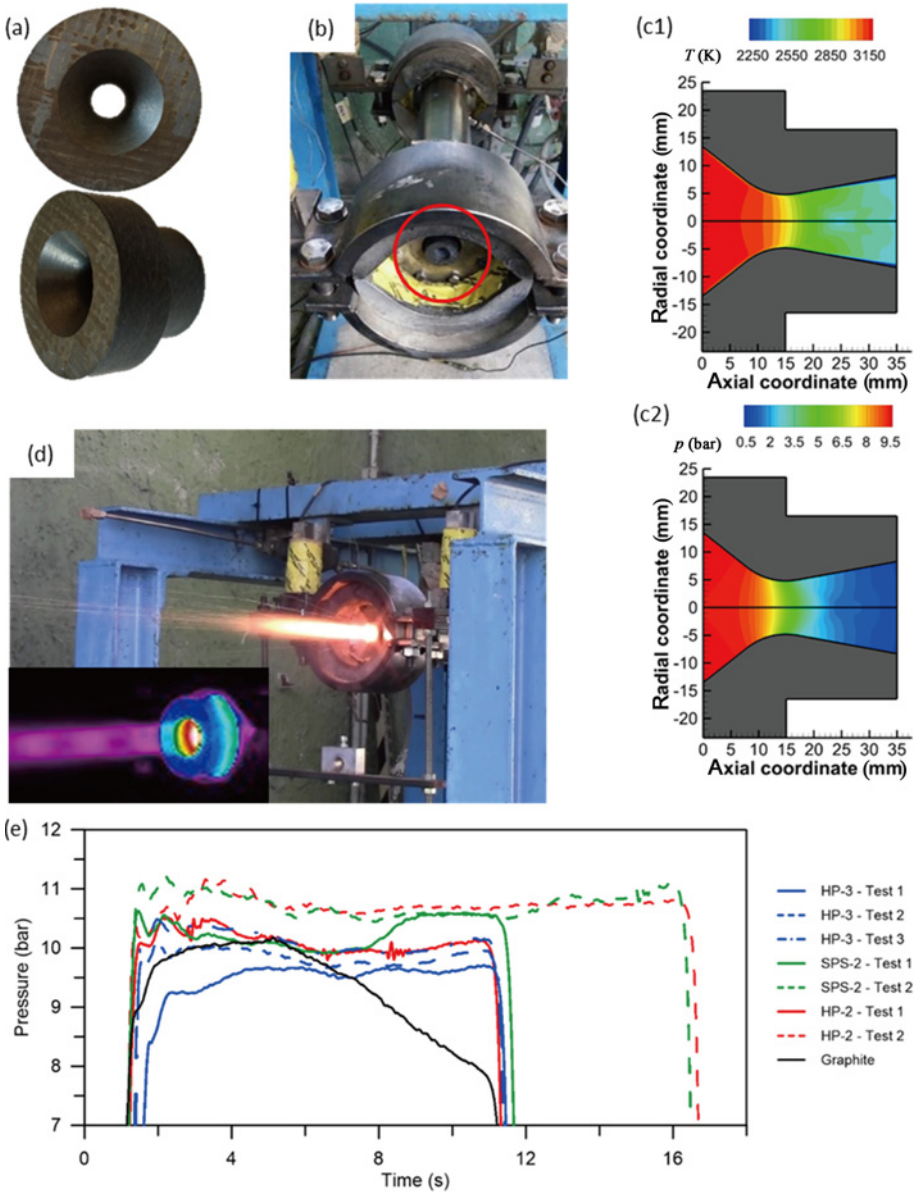

Fig. 4 (a) Nozzle before test, (b) hybrid motor mounted on test bench, (c) CFD-calculated distributions: (c1) static temperature and (c2) static pressure throughout nozzle in nominal test conditions, (d) nozzle exhaust plume during test (with an infrared thermo-camera (IR-TC) frame), and (e) combustion chamber pressure vs. time during firing tests on UHTCMC nozzles compared with reference graphite nozzle.

conditions achieved inside the combustion chamber and through the exhaust nozzle of rocket engines requires advanced materials highly resistant to chemical attack and to erosion at high temperatures.

The typical propulsion environment contains oxidizing chemical species, such as O_2, O, CO_2, and H_2O [60], resulting from the combustion reactions occurring in the chamber. These species are accelerated to supersonic Mach number through the nozzle, whose inner surface experiences the aero-thermo-chemical loads deriving from the tangential flow of the combusting mixture. The throat section, where a sonic Mach number is achieved, is the most solicited region, being subjected to the highest heat flux and shear stress, which may lead to consistent erosion, strong thermal gradient and thermal shock in the radial direction, and high tensile stresses in the longitudinal direction. Throat erosion causes a decrease in the combustion chamber pressure, which can directly affect motor thrust and specific impulse.

According to the numerical models described above, for the simulation of the flow field inside the considered hybrid rocket, the selected nominal test conditions correspond to a theoretical chamber pressure of 9.63 bar, a chamber temperature of 3200 K, and an O/F of 6.50, meaning that a significant amount of unburnt oxygen (a mass fraction over 0.40) is still available in the exhaust flow as an oxidizing agent. Throughout the nozzle, the combusting flow underwent an expansion to supersonic conditions, with a corresponding decrease in temperature and pressure, as verified by the contour plots of Fig. 4(c), obtained by means of the CFD simulations. Remarkably, the projected gas temperature is still in the order of 3000 K, and the pressure is over 6 bar in the throat region, where the cold-wall heat flux achieves its peak value of roughly 13 MW/m^2.

Figure 4(d) shows a picture taken during engine operation, highlighting the exhaust plume coming out of the nozzle and a thermo-graphic frame taken by means of an IR-TC (Thermacam P40, FLIR, Portland, USA; operating in the far-IR spectral range—8–14 μm).

The time histories of the pressure measured in the combustion chamber during all the tests are shown in Fig. 4(e), and compared with that of a reference graphite nozzle tested in the same conditions for 10 s. For all the tests, the pressure rose after roughly 1 s due to the ignition of the mixture, and then it reached a value close to the nominal one, keeping it steadily, and finally it dropped again when the oxygen feeding valve was electronically closed to shut down the engine.

For SPS-2, after about 8 s in the first run, a slight increase of the chamber pressure was recorded. Indeed, after the test, a reduction of the throat diameter was measured, from 9.6 mm to about 9.4 mm. For the same reason, during the second test, the measured chamber pressure was slightly higher than that in the first test. The observed shrinkage was caused by oxidation, as explained below. Similarly, for HP-2, after the first test, a slight reduction of the throat diameter, from 9.6 to 9.2 mm (on average) was measured, and this justifies the slight rise in chamber pressure during the second run. This final value of chamber pressure was also measured during the whole duration of the second test. For HP-3, no measurable erosion was observed, coherently with the stable pressure profile. It is interesting to notice that the conventional graphite nozzle, in such an oxidizing environment, was considerably eroded. Specifically, the throat diameter increased from 9.9 to 11.4 mm, resulting in a dramatic decrease in chamber pressure (roughly 7 bar at the end of the firing).

3.3 Post-test microstructural features

The nozzles were extracted intact from the rocket motors after the multiple tests. An example of the sectioned nozzle is shown in Fig. 5(a), where it is possible to see the different oxide layering in the inner walls of the throat. Due to the sharp angles of the prototype, the most stressed regions are the convergent part of the nozzle and the 90° corner of the machined sample. Microcracks starting from these corners were indeed observed after sectioning. As shown in Fig. 5(b), this observation was also predicted through the finite element method (FEM) developed during the EU project C^3HARME [61,62].

The pictures of the nozzle top view and details of the throat are shown in Fig. 6. As mentioned before, the throat sections maintained their original circular shape, with no visible erosion. White crusts and bulges can be noticed on the top views due to oxidation (Figs. 6(a)–6(c)). The optical microscopy images of the nozzles' inner part (Figs. 6(d)–6(f)) reveal a whitish surface, again due to oxidation phenomena. The extension of oxidation, covering both convergent and divergent part of the nozzle, is more pronounced for SPS-2 rather than HP-2. It is possible to observe a white crust with some darker stains, followed by a dark grey crust in the divergent part, which mainly consists of ZrO_2 and SiO_2, which will be discussed later. HP-3 was darker in appearance, likely due to the formation and coverage with extra SiO_2.

The details of the inner profiles are shown in Figs. 7–9 for SPS-2, HP-2, and HP-3, respectively. The SPS-2

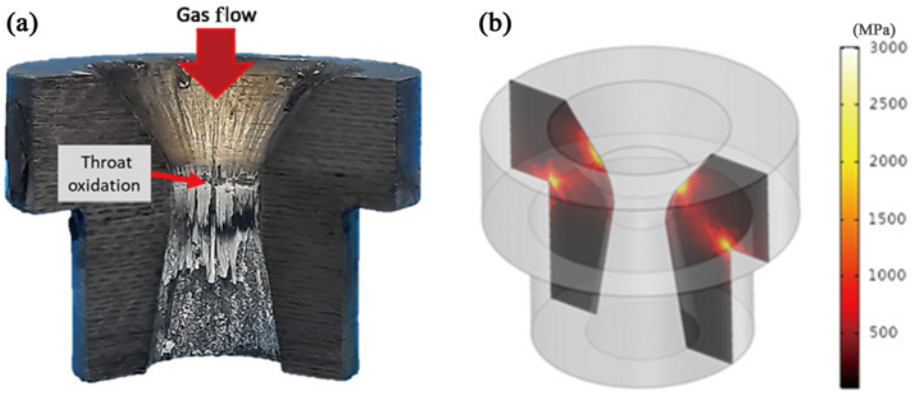

Fig. 5 (a) Camera picture of SPS-2 nozzle section after two consecutive tests and (b) projected thermal stresses, highlighting the most stressed regions, as estimated by COMSOL software.

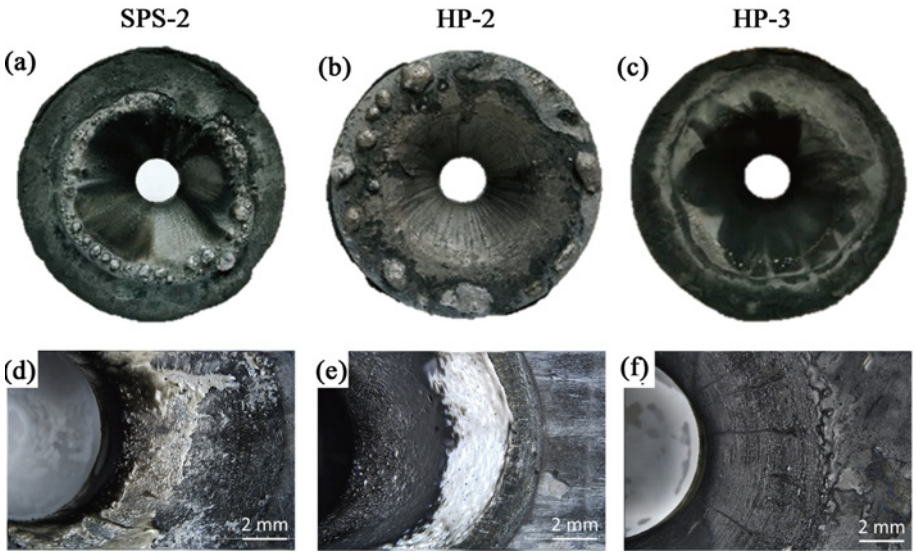

Fig. 6 Pictures of top views of specimens after all test sequences: (a) SPS-2, (b) HP-2, and (c) HP-3 and (d–f) details of their inner throats, respectively.

sample was characterized by a smooth inner surface profile mainly composed by a white layer, confirmed to be ZrO_2, together with a dark grey layer consisting of SiO_2 (Figs. 7(a) and 7(b), respectively). Looking at the details of the convergent and divergent parts of the sample obtained via SPS, it is possible to see the oxidized layer (Figs. 7(c) and 7(d)), which was 59±10 μm on average (Table 2). In this region, high gas temperature (3150 K), high pressure (10.5 bar), and relatively long gas residence time (due to the low Mach number upstream the throat) were achieved, with the cold-wall heat flux rising from 7 to 13 MW/m^2 and a maximum pressure of 11.0 bar. The cross section of the diverging part (Fig. 7(e)) does not show any significant oxidation or erosion in spite of the still harsh conditions calculated (gas temperature 2500 K, 1 bar, and 4 MW/m^2 at the nozzle exit), possibly also due to the relatively low gas residence time in the supersonic region, and both the fibers and the matrix were still intact (Fig. 7(f)).

This layer sequence has been already observed in Ref. [41] on the oxidation behavior of ZrB_2/SiC–C_f composites tested in a bottom–up furnace. The oxidation behavior observed here was comparable to that of the bottom–up furnace testing (1650 ℃, 1 bar, and static air), suggesting that the inner wall temperature reached in the nozzle was much lower than the gas temperature registered. Even the oxidized layer thickness (~59 μm) was comparable to that of a carbon fiber-reinforced ZrB_2+10%SiC composite (~57 μm) tested in the bottom–up furnace at 1650 ℃. The same material tested in a controlled environment at temperatures of 2000–2200 ℃ was considerably more damaged, and the protective SiO_2 layer was completely

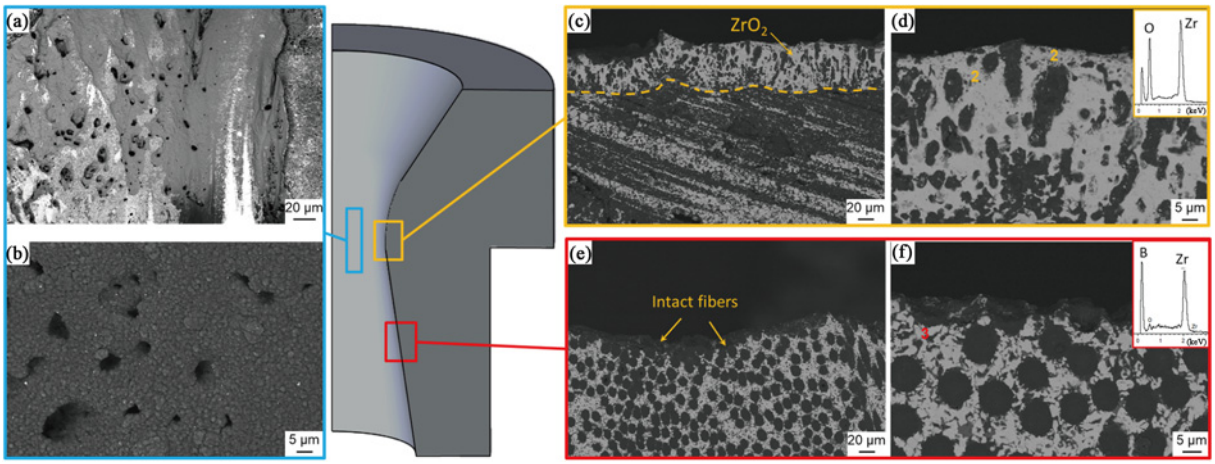

Fig. 7 Model of cross section of nozzle: (a, b) surfaces of inner throat of SPS-2 sample after testing, showing throat surface features, (c, d) cross sections of convergent part, and (e, f) cross sections of divergent part.

removed [63]. In that case, the oxidized layer thickness measured up to 300–400 μm. Remarkably, the surface of the divergent part was seemingly unaffected, as evidenced by the presence of unoxidized fibers and matrix (Figs. 7(e) and 7(f)), in spite of the projected very harsh conditions (gas temperature 2500 K and 1 bar). As argued above, due to the supersonic flow Mach number (higher than 2 at the nozzle exit), the real inner wall temperature of the nozzle was likely much lower than 2000 K. Moreover, the higher shear stresses (rising from 0 at over 3700 Pa in the convergent part, peaking at the throat section, and still higher than 1600 Pa at the nozzle exit) may have favoured liquid oxide removal during firing.

The HP-2 sample behaved very similarly to the SPS-2, although slightly less oxidized, as evidenced by the lower oxide thickness. These small differences may arise from the different process parameters of HP compared to those of SPS that affected the final porosity of the material. Indeed, the HP-2 sample was slightly less porous than SPS-2 (8.4% vs. 10.8% in porosity). In any case, both materials were characterized by very similar microstructures, and the oxidation behavior was comparable. From the SEM analysis on the surface of the throat, a mixture of white and grey oxides were observed, which were confirmed to be ZrO_2 and SiO_2, respectively (Figs. 8(a) and 8(b)). The fibers were still partly visible and were covered by SiO_2. Looking at the details of the convergent region (Figs. 8(c) and 8(d)), the surface was homogeneously covered with an oxide layer mainly consisting of small ZrO_2 particles embedded in SiO_2 in the thickness of 36±11 μm, while the divergent part did not show any signs of oxidation, and both the fibers and the matrix

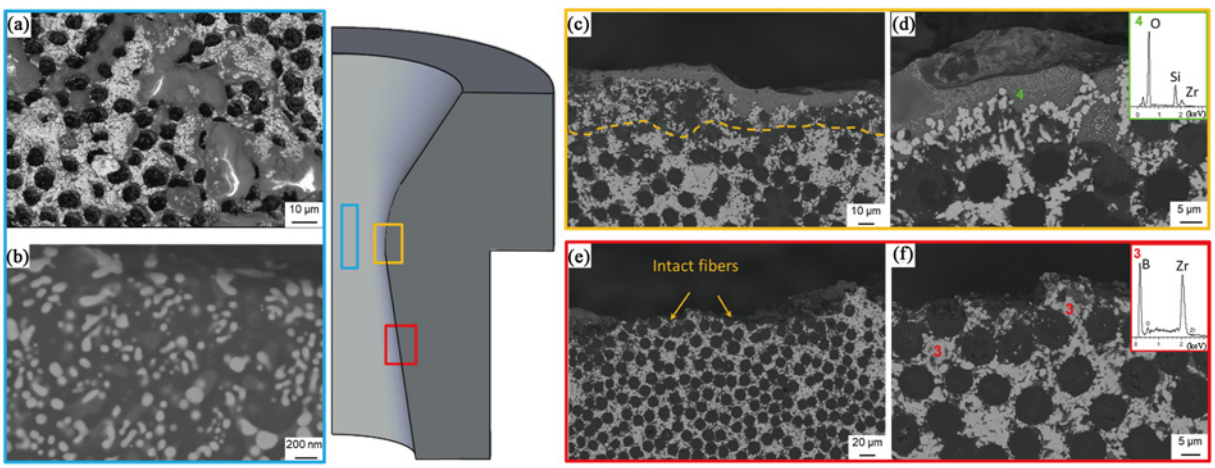

Fig. 8 Model of cross section of nozzle: (a, b) surfaces of inner throat of HP-2 sample after testing, showing surface features, (c, d) cross sections of convergent part, and (e, f) cross sections of divergent part.

were still intact (Figs. 8(e) and 8(f)). Depending on the analyzed area, SiO_2 was found with varying thicknesses, alternating with layers constituted mainly by ZrO_2, as seen for SPS-2.

The HP-3 sample was less porous (< 1%) than HP-2 (< 10%) (Table 2) due to the slightly higher sintering temperature and holding time, and it was characterized by a smooth profile of the tested surface, while the front view of the surface shows dark grey and white spots (Figs. 9(a) and 9(b), respectively). A lateral crack propagating from the edge was observed after the third test, which was likely derived from the repeated thermal shocks, causing high stress concentrations on the sharp edges, as previously foreseen by thermal stress simulation (Fig. 5(b)). The cross section showed a similar behavior to the other specimens, but in this case, the oxide layer appeared more porous. On further inspection of the convergent and divergent areas of the nozzle inner surface (Figs. 9(c) and 9(d)), the majority of the oxidation took place in the convergent region, with the formation of an outer ZrO_2–SiO_2 layer and an intermediate porous ZrO_2 layer, while the divergent region was apparently unaffected with intact fibers (Fig. 9(e)) and unoxidized ZrB_2 (Fig. 9(f)). The progressive oxidation of ZrB_2/SiC to ZrO_2–SiO_2, followed by the impoverishment of the matrix and the formation of the porous intermediate layer, has been previously documented and is a phenomenon encountered during prolonged exposure in highly oxidizing environments at high temperatures.

3. 4 Oxidation behavior mechanism

Although the gas temperature during test can reach 3000 K, as indicated by predictions, the nozzle wall certainly was at lower temperatures. Precise estimation of wall temperature is complex because the phenomenon is highly unsteady, and the surface evolution in different thermal cycles also depends on the material response itself. It is reasonable to assume that in the whole area of the convergent up to the throat, a wall temperature between 1500 and 2000 K in the longest tests was reached. In order to provide an estimate of the temperatures achieved on the materials surface, three transient simulations of the nozzle thermal behavior were carried out by means of the model described in Section 2. In the first simulation, the whole material was assigned orthotropic and temperature-dependent thermal properties (specific heat and thermal conductivity plus constant density) according to the data in Table 1. The surface emissivity was set to 0.85. This case was labelled as "Unoxidized". In the second and third simulations, the presence of a 60 μm-thick oxide layer over the whole nozzle inner surface was taken into account. In the second simulation (Oxidized-k = 2 W/(m·K)), this layer was characterized by a specific heat equal to 650 J/(kg·K) and a thermal conductivity of 2 W/(m·K), according to Ref. [37]. In the third simulation (Oxidized-k = 1 W/(m·K)), for an additional parametric analysis taking possible factors into account, leading to the reduction in thermal conduction through the oxide, such as porosity, the oxide layer thermal conductivity was set to 1 W/(m·K) [64–66]. In both the simulations with the oxide layer, the nozzle inner surface emissivity was set to 0.5 [64]. In all the simulations, the temperature field was initialized to 300 K in the whole solid domain, and the simulation lasted 15 s.

Figure 10 shows the evolution of the maximum

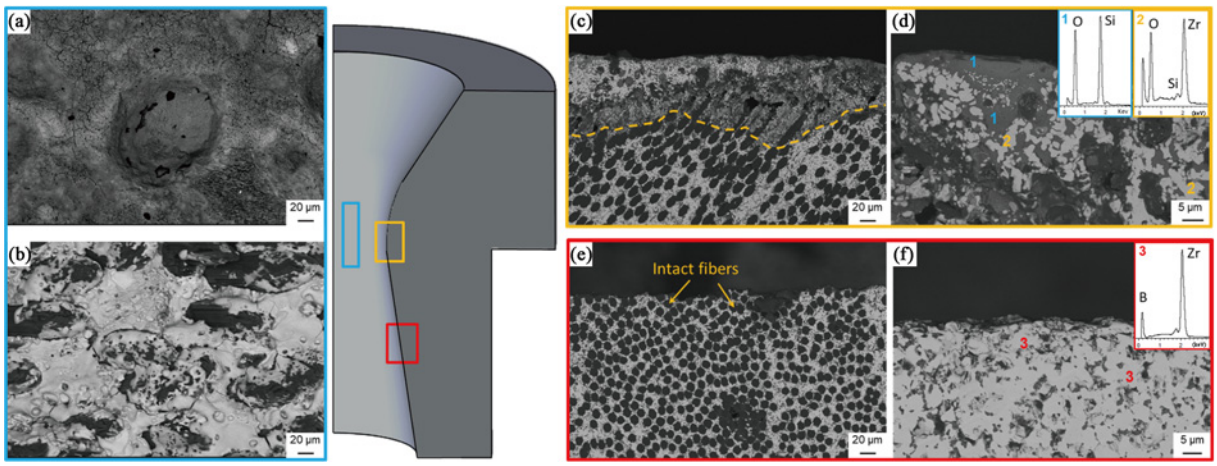

Fig. 9 Model of cross section of nozzle: (a, b) surfaces of inner throat of HP-3 sample after testing, showing surface features, (c, d) cross sections of convergent part, and (e, f) cross sections of divergent part.

temperature reached by the nozzle inner surface in the three cases. The temperature is evaluated as the maximum reached in any point of the surface at each time instant. This is located for all test duration in close proximity of the throat section. It is possible to observe that the presence of the oxide layer, as expected, causes a shift in the maximum surface temperature by a few hundred Kelvin degree, with the main factor residing in the modified thermal conductivity. It is worth remarking that this is mostly a parametric analysis, since in such short-duration, unsteady tests, an actual steady state of the oxidation process is presumably never reached, so the surface behavior is expected to have migrated from the blue ("Unoxidized") curve to one of the "Oxidized" curves during the firing themselves. Also, in reusability tests, the initial oxide conditions may have differed from firing to firing. However, these computations provide an estimate of the achieved surface temperatures (ranging from 1600 to 1900 K at the end of the longest firing) in support of the present discussion.

According to thermodynamic simulations carried out with Factsage 8.0 software, the main oxidation products at 2000 K and 9.5 bar are t-ZrO_2, liquid SiO_2–B_2O_3, and volatile oxides, such as CO, CO_2, SiO, B_2O_3, BO, B_2O, and BO_2. The SiO_2, at these high pressures, is still present on the surface as a viscous liquid layer. Due to the high flow rates of the oxygen/fuel, part of this melt is hypothesized to flow along the throat and coat the lower area of the throat; the evidence of this phenomenon can be found in Fig. 11, where a dark grey crust was visibly spread on top of the unoxidized material. This smeared silica layer was likely responsible for the protection of the material below.

Since this smeared coating was not chemically bonded to the substrate, it likely came off during the polishing procedure, which exposed the unoxidized material below. The shrinkage of the throat section that was measured just after some of the firing tests may be linked to the deposition of this ZrO_2–SiO_2 layer. In Refs. [64,67] on the same material tested in an arc-jet environment, in fact, the oxidation process led to a slight thickening of materials samples, coherently with the present results. In Ref. [68] on the ablation resistance of C–ZrC/SiC and C–ZrB_2/SiC composites tested at 1800 ℃, a similar oxide layering was observed, with the formation of an outer ZrO_2–SiO_2 scale and an intermediate porous layer; but in this case, the outer layer was prone to peeling off, exposing the underlying unoxidized structure. In that case, only employing an outer layer of ZrB_2–SiC, it was possible to avoid the oxide peeling off [69]. In our case, the

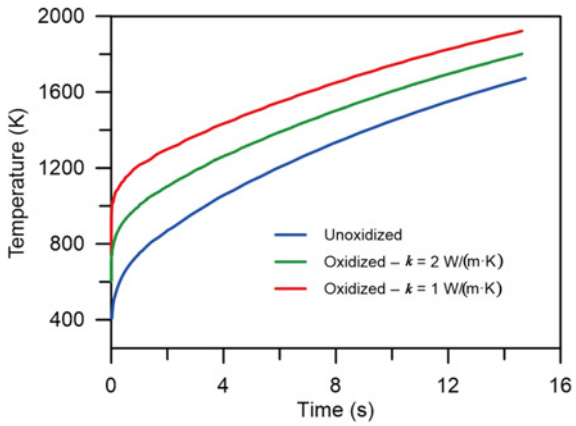

Fig. 10 Maximum temperatures achieved in time over inner surface of the nozzles for different material properties calculated by the CFD.

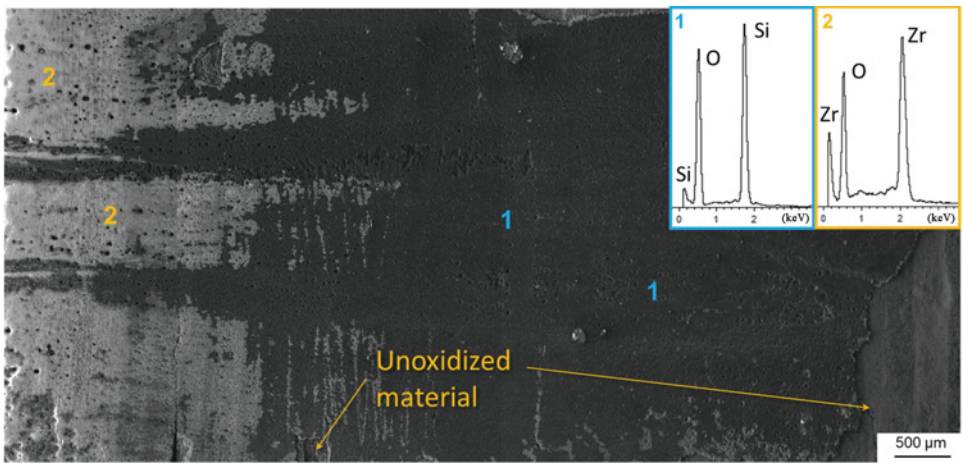

Fig. 11 Low-magnification micrograph showing surficial crust constituted by SiO_2–ZrO_2 spread along the length of the throat.

outer layer was preserved, and no peeling off was observed without the need of successive layer deposition. Combining these new findings with the results obtained from our previous works, the following oxidation mechanism was proposed: In the range of 700–1000 ℃, the oxidation of the fibers and boride matrix is kinetically favoured compared to the formation of the protective silica layer, leading to the initial oxidation of the outer fibers and the formation of ZrO_2 and B_2O_3. With the increasing temperature above 1200 ℃, the evolution of boron oxides and the oxidation of SiC to SiO_2 is promoted, leading to the passivation of the outer layer and the formation of a ZrO_2–SiO_2 scale that provides protection up to 1700 ℃. However, as discussed above, the action of high local gas pressures can lead to the displacement of the glassy SiO_2 layer, resulting in the formation of two regions with varying SiO_2 coverage (Fig. 12(b)).

3. 5 Comparison with state-of-the-art materials

Erosion resistant nozzles that can maintain dimensional stability during firing are required for more demanding propulsion applications. The state-of-the-art materials used for these applications include refractory metals, refractory-metal carbides, graphite, ceramics, and fiber-reinforced plastics [5], but the choice depends on the specific application. Fully densified refractory-metal nozzles are generally more resistant to erosion and thermal-stress cracking than the other materials. Graphite performs well with the least oxidizing propellant but is severely eroded in the process.

It is worth noticing that in the same or even under less demanding conditions, conventional graphite nozzles showed a visible decrease in the chamber pressure, due to considerable throat thermo-chemical erosion [70,71], as demonstrated by the reference test on graphite shown in Fig. 4(e).

Some of the refractory-metal carbide nozzles are reported to show outstanding erosion resistance, comparable to that of the best refractory-metal materials, but generally suffer due to fractures induced by thermal stresses. A nozzle made of monolithic tantalum carbide was previously manufactured with the same geometry of the present nozzles. Although no erosion was observed, the nozzle failed catastrophically after the first run due to its intrinsic brittleness and low thermal shock resistance [70,71].

UHTCMC nozzles were at the same time damage tolerant (the formation of microcracks in the most stresses areas did not compromise the tests) and resistant to erosion. This work demonstrated how these advanced structural ceramic composites can achieve

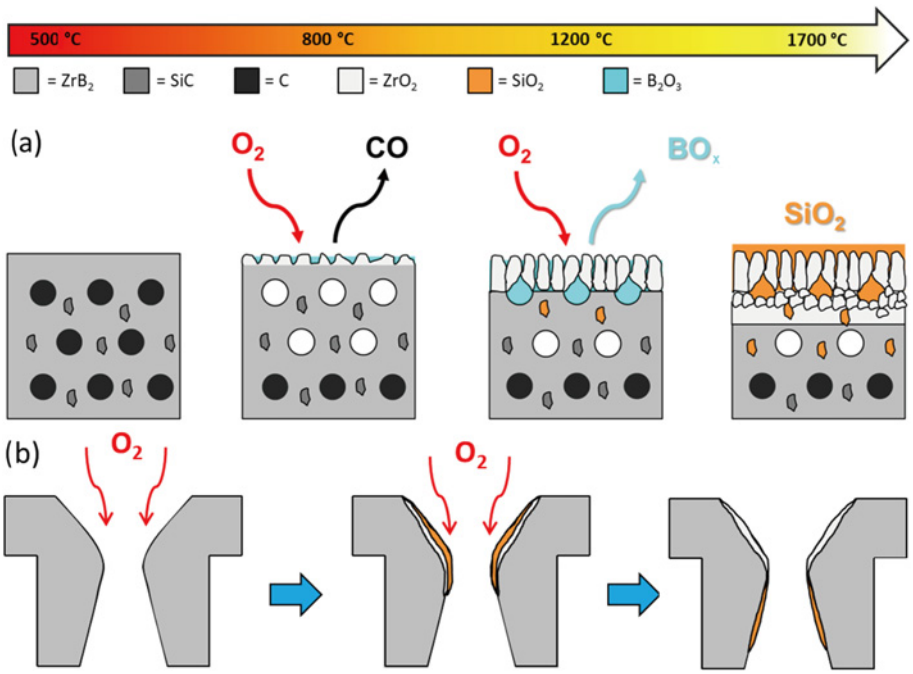

Fig. 12 (a) Oxidation phenomena from RT to 1700 ℃: oxidation of outer fibers and ZrB_2 to CO, ZrO_2, and B_2O_3, evaporation of boron oxides and formation of SiO_2, and formation of ZrO_2–SiO_2 scale. (b) Ablation mechanism in nozzle: The convergent part of the nozzle is exposed to the highest static temperature at relatively high gas residence time and is rapidly oxidized to ZrO_2 and liquid SiO_2. The silica, having lower viscosity, is displaced and spread towards the diverging part of the nozzle.

unprecedented levels of safe operation of reusable components for aerospace propulsion. The addition of fiber-reinforcement did not degrade the refractory properties, and the densification of the ceramic matrix, through the sintering process, did not reduce the structural properties. This successful integration between fiber and UHTC matrix allowed to produce a nozzle that did not fail during the thermal excursion experienced by the engine, and can allow to produce reusable components for aerospace propulsion.

4 Conclusions

In this paper, the reusability of UHTCMC-based nozzles for rocket propulsion was assessed by repeatedly testing the same nozzle in a hybrid rocket motor. All specimens were obtained by sintering (either from HP or SPS) and had slight variations in behavior, which was mostly affected by porosity. Compared to a reference graphite nozzle, no erosion was observed for the UHTCMC-based nozzles; instead, a decrease of diameter of the throat was observed, which resulted in a slight increase of pressure on the inner walls.

In spite of the high gas temperatures registered (> 3000 K), the observed oxidation behavior was similar to that of specimens tested at 1500–1650 ℃ in an air furnace, suggesting that the real temperatures inside the nozzles were likely 2000 K or lower, as supported by numerical simulations.

The oxidation mechanism consisted in the formation of a ZrO_2 intermediate layer, with a liquid SiO_2 layer on the surface that was displaced by the action of the gas flux towards the divergent part of the nozzle, protecting it from further oxidation. Repeated testing actually led to a decrease of the throat diameter, possibly due to the formation of a liquid oxide layer during firing with a lower density.

These tests demonstrated the capability of complex-shaped prototypes made of the developed UHTCMC to survive repeated exposure to a harsh environment representative of a realistic space propulsion application, for overall operating time up to 30 s, without any failures nor measurable erosion, making a promising step towards the development of reusable rocket components. Future studies will address the capability of these materials to withstand prolonged exposure time in oxidizing conditions or a high number of oxidation cycles in short succession.

Acknowledgements

This work received support by the EU's Horizon 2020 research and innovation programme under Grant No. 685594 (C^3HARME: Next Generation Ceramic Composites for Harsh Combustion Environment and Space), and project CARBOSPACE (Ultrarefractory Ceramic Composites for Aerospace Defense Transport Energy).

Declaration of competing interest

The authors have no competing interests to declare that are relevant to the content of this article.

References

[1] Drenthe NT, Zandbergen BTC, Curran R, *et al*. Cost estimating of commercial smallsat launch vehicles. *Acta Astronaut* 2019, **155**: 160–169.
[2] Mungiguerra S, Di Martino GD, Zuppardi G. Computational evaluation of aero-thermodynamic loads and effect of catalyticity in an arc-jet wind tunnel. *J Aerospace Eng* 2020, **33**: 04020005.
[3] Sutton GP, Bibliarz O. *Rocket Propulsion Elements*, 7th edn. Hoboken, USA: John Wiley & Sons, 2001.
[4] Savino R, Mungiguerra S, Di Martino GD. Testing ultra-high-temperature ceramics for thermal protection and rocket applications. *Adv Appl Ceram* 2018, **117**: s9–s18.
[5] Evans B, Kuo KK, Cortopassi AC. Characterization of nozzle erosion behavior under rocket motor operating conditions. *Int J Energ Mater Ch* 2010, **9**: 533–548.
[6] Padture NP. Advanced structural ceramics in aerospace propulsion. *Nat Mater* 2016, **15**: 804–809.
[7] He QC, Li HJ, Tan Q, *et al*. Effects of ZrC particle size on ablation behavior of C/C–SiC–ZrC composites prepared by chemical liquid vapor deposition. *Corros Sci* 2022, **205**: 110469.
[8] He QC, Li HJ, Tan Q, *et al*. Influence of carbon preform density on the microstructure and ablation resistance of CLVD-C/C–ZrC–SiC composites. *Corros Sci* 2021, **190**: 109648.
[9] He QC, Li HJ, Yin XM, *et al*. Effects of PyC shell thickness on the microstructure, ablation resistance of SiCnws/PyC–C/C–ZrC–SiC composites. *J Mater Sci Technol* 2021, **71**: 55–66.
[10] Zeng Y, Wang DN, Xiong X, *et al*. Ablation-resistant carbide $Zr_{0.8}Ti_{0.2}C_{0.74}B_{0.26}$ for oxidizing environments up to 3,000 ℃. *Nat Commun* 2017, **8**: 15836.
[11] Du BH, Cheng Y, Xun LC, *et al*. Using PyC modified 3D carbon fiber to reinforce UHTC under low temperature sintering without pressure. *J Adv Ceram* 2021, **10**: 871–884.
[12] Ni DW, Cheng Y, Zhang JP, *et al*. Advances in ultra-high temperature ceramics, composites, and coatings. *J Adv Ceram* 2022, **11**: 1–56.

[13] Galizia P, Failla S, Zoli L, *et al*. Tough salami-inspired C_f/ZrB_2 UHTCMCs produced by electrophoretic deposition. *J Eur Ceram Soc* 2018, **38**: 403–409.
[14] Zhang DY, Hu P, Dong S, *et al*. Effect of pyrolytic carbon coating on the microstructure and fracture behavior of the C_f/ZrB_2–SiC composite. *Ceram Int* 2018, **44**: 19612–19618.
[15] Galizia P, Sciti D, Saraga F, *et al*. Off-axis damage tolerance of fiber-reinforced composites for aerospace systems. *J Eur Ceram Soc* 2020, **40**: 2691–2698.
[16] Zoli L, Sciti D. Efficacy of a ZrB_2–SiC matrix in protecting C fibres from oxidation in novel UHTCMC materials. *Mater Design* 2017, **113**: 207–213.
[17] Sciti D, Silvestroni L, Monteverde F, *et al*. Introduction to H2020 project C^3HARME—Next generation ceramic composites for combustion harsh environment and space. *Adv Appl Ceram* 2018, **117**: s70–s75.
[18] Mungiguerra S, Di Martino GD, Cecere A, *et al*. Arc-jet wind tunnel characterization of ultra-high-temperature ceramic matrix composites. *Corros Sci* 2019, **149**: 18–28.
[19] Mungiguerra S, Di Martino GD, Savino R, *et al*. Ultra-high-temperature ceramic matrix composites in hybrid rocket propulsion environment. In: Proceedings of the 2018 International Energy Conversion Engineering Conference, Cincinnati, USA, 2018: AIAA 2018-4694.
[20] Rubio V, Binner J, Cousinet S, *et al*. Materials characterisation and mechanical properties of C_f–UHTC powder composites. *J Eur Ceram Soc* 2019, **39**: 813–824.
[21] Yan CL, Liu RJ, Cao YB, *et al*. Preparation and properties of 3D needle-punched C/ZrC–SiC composites by polymer infiltration and pyrolysis process. *Ceram Int* 2014, **40**: 10961–10970.
[22] Wu HT, Xie CM, Zhang WG, *et al*. Fabrication and properties of 2D C/C–ZrB_2–ZrC–SiC composites by hybrid precursor infiltration and pyrolysis. *Adv Appl Ceram* 2013, **112**: 366–373.
[23] Galizia P, Sciti D, Jain N. Insight into microstructure and flexural strength of ultra-high temperature ceramics enriched SICARBON^{TM} composite. *Mater Design* 2021, **208**: 109888.
[24] Li Y, Chen S, Ma X, *et al*. Influence of preparation temperature on the properties of C/ZrC composites. *J Alloys Compd* 2017, **690**: 206–211.
[25] Yan CL, Liu RJ, Zhang CR, *et al*. Effects of SiC/HfC ratios on the ablation and mechanical properties of 3D C_f/HfC–SiC composites. *J Eur Ceram Soc* 2017, **37**: 2343–2351.
[26] Zhang XH, Du BH, Hu P, *et al*. Thermal response, oxidation and ablation of ultra-high temperature ceramics, C/SiC, C/C, graphite and graphite–ceramics. *J Mater Sci Technol* 2022, **102**: 137–158.
[27] Paul A, Venugopal S, Binner JGP, *et al*. UHTC–carbon fibre composites: Preparation, oxyacetylene torch testing and characterisation. *J Eur Ceram Soc* 2013, **33**: 423–432.
[28] Paul A, Rubio V, Binner J, *et al*. Evaluation of the high temperature performance of HfB_2 UHTC particulate filled C_f/C composites. *Int J Appl Ceram Technol* 2017, **14**: 344–353.
[29] Sayir A. Carbon fiber reinforced hafnium carbide composite. *J Mater Sci* 2004, **39**: 5995–6003.
[30] Wang Z, Dong SM, Zhang XY, *et al*. Fabrication and properties of C_f/SiC–ZrC composites. *J Am Ceram Soc* 2008, **91**: 3434–3436.
[31] Li QG, Dong SM, Wang Z, *et al*. Fabrication and properties of 3-D C_f/ZrB_2–ZrC–SiC composites via polymer infiltration and pyrolysis. *Ceram Int* 2013, **39**: 5937–5941.
[32] Vignoles GL. Chemical vapor deposition/infiltration processes for ceramic composites. In: *Advances in Composites Manufacturing and Process Design*. Philippe B, Ed. Amsterdam, the Netherlands: Woodhead Publishing, 2015: 147–176.
[33] Chen S, Zhang CR, Zhang YD, *et al*. Preparation and properties of carbon fiber reinforced ZrC–ZrB_2 based composites via reactive melt infiltration. *Compos Part B-Eng* 2014, **60**: 222–226.
[34] Pi HL, Fan SW, Wang YG. C/SiC–ZrB_2–ZrC composites fabricated by reactive melt infiltration with $ZrSi_2$ alloy. *Ceram Int* 2012, **38**: 6541–6548.
[35] Vinci A, Zoli L, Galizia P, *et al*. Reactive melt infiltration of carbon fibre reinforced ZrB_2/B composites with Zr_2Cu. *Compos Part A-Appl S* 2020, **137**: 105973.
[36] C³HARME. Available at https://c3harme.eu/.
[37] Galizia P, Vinci A, Zoli L, *et al*. Retained strength of UHTCMCs after oxidation at 2278 K. *Compos Part A-Appl S* 2021, **149**: 106523.
[38] Zoli L, Vinci A, Galizia P, *et al*. Is spark plasma sintering suitable for the densification of continuous carbon fibre—UHTCMCs? *J Eur Ceram Soc* 2020, **40**: 2597–2603.
[39] Zoli L, Vinci A, Galizia P, *et al*. On the thermal shock resistance and mechanical properties of novel unidirectional UHTCMCs for extreme environments. *Sci Rep* 2018, **8**: 9148.
[40] Fahrenholtz WG, Hilmas GE, Talmy IG, *et al*. Refractory diborides of zirconium and hafnium. *J Am Ceram Soc* 2007, **90**: 1347–1364.
[41] Vinci A, Zoli L, Sciti D. Influence of SiC content on the oxidation of carbon fibre reinforced ZrB_2/SiC composites at 1500 and 1650 ℃ in air. *J Eur Ceram Soc* 2018, **38**: 3767–3776.
[42] Sciti D, Zoli L, Reimer T, *et al*. A systematic approach for horizontal and vertical scale up of sintered Ultra-High Temperature Ceramic Matrix Composites for aerospace—Advances and perspectives. *Compos Part B-Eng* 2022, **234**: 109709.
[43] Medri V, Capiani C, Gardini D. Slip casting of ZrB_2–SiC composite aqueous suspensions. *Adv Eng Mater* 2010, **12**: 210–215.
[44] Di Martino GD, Mungiguerra S, Carmicino C, *et al*. Two-hundred-Newton laboratory-scale hybrid rocket testing for paraffin fuel-performance characterization. *J Propul Power* 2019, **35**: 224–235.
[45] Mungiguerra S, Di Martino GD, Savino R, *et al*. Characterization of novel ceramic composites for rocket nozzles in high-temperature harsh environments. *Int J Heat Mass Tran* 2020, **163**: 120492.

[46] Sciti D, Zoli L, Silvestroni L, *et al*. Design, fabrication and high velocity oxy-fuel torch tests of a C_f–ZrB_2-fiber nozzle to evaluate its potential in rocket motors. *Mater Design* 2016, **109**: 709–717.
[47] Di Martino GD, Mungiguerra S, Cecere A, *et al*. Hybrid rockets with nozzle in ultra-high-temperature ceramic composites. In: Proceedings of the 69th International Astronautical Congress, Bremen, Germany, 2018: IAC-18,C4,3,6,x47333.
[48] Chorin AJ. Numerical solution of the Navier–Stokes equations. *Math Comput* 1968, **22**: 745–762.
[49] Menter FR. Two-equation eddy-viscosity turbulence models for engineering applications. *AIAA J* 1994, **32**: 1598–1605.
[50] Magnussen B. On the structure of turbulence and a generalized eddy dissipation concept for chemical reaction in turbulent flow. In: Proceedings of the 19th Aerospace Sciences Meeting, St. Louis, USA, 1981: AIAA 1981-42.
[51] Modest MF. *Radiative Heat Transfer*, 2nd edn. Amsterdam, the Netherlands: Academic Press, 2003.
[52] Galizia P, Sciti D. Disclosing residual thermal stresses in UHT fibre-reinforced ceramic composites and their effect on mechanical behaviour and damage evolution. *Compos Part B-Eng* 2023, **248**: 110369.
[53] Galizia P, Zoli L, Sciti D. Impact of residual stress on thermal damage accumulation, and Young's modulus of fiber-reinforced ultra-high temperature ceramics. *Mater Design* 2018, **160**: 803–809.
[54] Monteverde F, Guicciardi S, Bellosi A. Advances in microstructure and mechanical properties of zirconium diboride based ceramics. *Mater Sci Eng A* 2003, **346**: 310–319.
[55] Pradere C, Sauder C. Transverse and longitudinal coefficient of thermal expansion of carbon fibers at high temperatures (300–2500 K). *Carbon* 2008, **46**: 1874–1884.
[56] Sciti D, Zoli L, Vinci A, *et al*. Effect of PAN-based and pitch-based carbon fibres on microstructure and properties of continuous C_f/ZrB_2–SiC UHTCMCs. *J Eur Ceram Soc* 2021, **41**: 3045–3050.
[57] Schäfer W, Vogel WD. Faserverstärkte keramiken hergestellt durch polymerinfiltration. In: *Keramische Verbundwerkstoffe*. Walter K, Ed. Weinheim, Germany: Wiley-VCH Verlag GmbH, 2002: 76–94. (in German)
[58] SGL Carbon. SIGRASIC® carbon fiber reinforced silicon carbide. Available at https://www.sglcarbon.com/en/markets-solutions/material/sigrasic-carbon-fiber-reinforced-silicon-carbide/, 2023.
[59] Krenkel W. Carbon fibre reinforced silicon carbide composites (C/SiC, C/C–SiC). In: *Handbook of Ceramic Composites*. Bansal NP, Ed. New York, USA: Springer New York, 2005: 117–148.
[60] Savino R, Criscuolo L, Di Martino GD, *et al*. Aero-thermo-chemical characterization of ultra-high-temperature ceramics for aerospace applications. *J Eur Ceram Soc* 2018, **38**: 2937–2953.
[61] Jain N, Sanvito S. Specific set of recommendation for materials development in WP2 based on micro-models/DFT. Report of Deliverable 3.7, C^3HARME Project, 2017: 685594. Available at https://c3harme.eu/wp-content/uploads/2018/02/C3_D3.7.pdf.
[62] Reimer T, Esser B, Mungiguerra S, *et al*. Next generation ceramic composites for combustion harsh environments and space. Periodical Technical Report Part B: WP3, 2020: 47–50. Available at https://cordis.europa.eu/project/id/685594/results/it.
[63] Vinci A, Reimer T, Zoli L, *et al*. Influence of pressure on the oxidation resistance of carbon fiber reinforced ZrB_2/SiC composites at 2000 and 2200 ℃. *Corros Sci* 2021, **184**: 109377.
[64] Mungiguerra S, Di Martino GD, Cecere A, *et al*. Ultra-high-temperature testing of sintered ZrB_2-based ceramic composites in atmospheric re-entry environment. *Int J Heat Mass Tran* 2020, **156**: 119910.
[65] Mungiguerra S, Cecere A, Savino R, *et al*. Improved aero-thermal resistance capabilities of ZrB_2-based ceramics in hypersonic environment for increasing SiC content. *Corros Sci* 2021, **178**: 109067.
[66] Nait-Ali B, Haberko K, Vesteghem H, *et al*. Thermal conductivity of highly porous zirconia. *J Eur Ceram Soc* 2006, **26**: 3567–3574.
[67] Mungiguerra S, Silvestroni L, Savino R, *et al*. Qualification and reusability of long and short fibre-reinforced ultra-refractory composites for aerospace thermal protection systems. *Corros Sci* 2022, **195**: 109955.
[68] Cheng Y, Lyu Y, Xie YS, *et al*. Starting from essence to reveal the ablation behavior and mechanism of 3D PyC C_f/ZrC–SiC composite. *Corros Sci* 2022, **201**: 110261.
[69] Cheng Y, Liu C, Hu P, *et al*. Using *in-situ* conversed nano SiC to bond UHTC particles and construct anti-ablation coating. *Compos Part A-Appl S* 2022, **162**: 107159.
[70] Savino R, Festa G, Cecere A, *et al*. Experimental set up for characterization of carbide-based materials in propulsion environment. *J Eur Ceram Soc* 2015, **35**: 1715–1723.
[71] Di Martino GD, Mungiguerra S, Cecere A, *et al*. Ultra-high-temperature ceramic matrix composites for hybrid rocket nozzles. 2019. Available at https://www.iris.unina.it/handle/11588/779636.